A Novel Characterization of Seismic Site Response: Time–Frequency Transfer Function

Miriam Kristekova[1,2], Peter Moczo*[1,2], Jozef Kristek[1,2], Pierre-Yves Bard[3], Niloufar Babaadam[1], and Martin Galis[1,2]

ABSTRACT

Fourier transfer function FTF(*f*), defined as a Fourier transform of the impulse response of the medium between a source and receiver, fully characterizes transfer properties in the frequency domain. Modulus of FTF(*f*) is one of the most used characteristics of seismic site response in both theoretical and numerical analyses of effects of local surface structures on seismic motion. It is especially useful for identifying resonance peaks and/or the amplified frequency bands. By definition, however, |FTF(*f*)| cannot provide information on temporal development of the site response. In this article, we introduce a novel characterization of seismic site response—time–frequency transfer function TFTF(*t*, *f*) that properly characterizes temporal development of frequency content of transfer function. This feature significantly helps in interpretating wavefield composition. We present theory that is readily applicable to any time-dependent output signal. We demonstrate superior properties of TFTF(*t*, *f*) in comparison with standard |FTF(*f*)| for selected quasi-1D canonical models of local surface sedimentary structures. In the model of a semi-infinite layer, TFTF(*t*, *f*) made it possible to distinguish modes of vertical resonance and modes of surface waves, which is impossible based on standard |FTF(*f*)|.

KEY POINTS

- We introduce a novel characterization of seismic site response—time–frequency transfer function (TFTF).
- We demonstrate unique and useful TFTF properties for site response of local sedimentary structures.
- TFTF is applicable to a broad range of applications based on transfer function analysis.

INTRODUCTION

As is well known, the complex Fourier transfer function FTF(*f*) is the Fourier spectrum of the impulse response (IR) of the medium between a source and receiver, assuming the strictly Dirac impulse as a source time function (e.g., Paolucci, 1999; Moczo *et al.*, 2018; among many others). Therefore, FTF(*f*) fully characterizes (linear, time-invariant) transfer properties of the medium between the source and receiver in the frequency domain.

Its modulus |FTF(*f*)| is one of the most used characteristics in analysis of seismic site response. It shows frequency-dependent amplification or deamplification of the seismic signal due to propagation between the location of a control point, that is, a local bedrock motion, and receiver. At the same time, |FTF(*f*)| does not show the temporal development of the response. Although the complex FTF(*f*) contains phase information related to timing, this information is not displayed in the amplitude spectrum and is difficult to interpret directly in terms of evolving wavefield components. Despite various attempts (e.g., Ohsaki, 1979; Nigam, 1984; Sawada, 1984; Boore, 2003; Beauval *et al.*, 2003; Birgören and Irikura, 2005), no method to infer and include temporal development of the site response is routinely used in engineering seismology practice.

The missing phase information does not pose a problem for simple nearly 1D conditions because modal interpretation is often straightforward from resonance peaks alone. For laterally heterogeneous structures, however, physically distinct contributions may overlap in frequency while remaining separated in time. This is especially relevant for site-response problems in which later arrivals are associated with basin-edge effects, locally generated Love waves, or scattering from irregular interfaces (e.g., Moczo and Bard, 1993; Kawase, 1996; Molina-Villegas *et al.*, 2018).

1. Faculty of Mathematics, Physics and Informatics, Comenius University in Bratislava, Bratislava, Slovakia, https://orcid.org/0000-0001-9017-5952 (MK); https://orcid.org/0000-0001-5276-9311 (PM); https://orcid.org/0000-0002-2332-541X (JK); https://orcid.org/0000-0002-8426-5887 (NB); https://orcid.org/0000-0002-5375-7061 (MG); 2. Earth Science Institute, Slovak Academy of Sciences, Bratislava, Slovakia; 3. ISTerre, University Grenoble Alpes, University Savoie Mont Blanc, CNRS, IRD, University Gustave Eiffel, Grenoble, France, https://orcid.org/0000-0002-3018-1047 (P-YB)

*Corresponding author: moczo@fmph.uniba.sk

Cite this article as Kristekova, M., P. Moczo, J. Kristek, P.-Y. Bard, N. Babaadam, and M. Galis (2026). A Novel Characterization of Seismic Site Response: Time–Frequency Transfer Function, *Bull. Seismol. Soc. Am.* **XX**, 1–12, doi: 10.1785/0120260069

It is very natural and reasonable to assume that the missing phase information could be useful for interpreting complicated resulting motions in local surface structures. Wavefields in local structures are complex due to multiple wave reflections and transmissions, conversions, interference, diffraction, scattering, and resonance. These phenomena lead to later, secondary arrivals that can have a clearer signature in the time–frequency (TF) domain than in the sole frequency domain.

The TF representation (TFR) of a signal has already proved very useful in many studies in various fields of research. In seismology, they include a wide range of applications as the analysis of strong ground motion, quantitative comparison of synthetic and observed signals, identification of overlapping seismic phases, time-domain analysis of site-response-related signals, polarization analysis, denoising and designaling, and seismic interferometry (see, e.g., Rial, 1996; Basokur *et al.*, 2003; Birgören and Irikura, 2005; Kristekova, Kristek, Moczo, and Day, 2006, 2008, 2009; Burjánek *et al.*, 2010; Poggi *et al.*, 2012; Yamamoto and Baker, 2013; Chaljub *et al.*, 2015; Kuyuk, 2015; Maufroy *et al.*, 2015, 2016; Bonilla *et al.*, 2019; Yang *et al.*, 2020; Aguiar *et al.*, 2026; among many others).

In general, different methods can be used to obtain the TFR of a signal. Because of their favorable properties, the continuous wavelet transform (CWT), often implemented using the Morlet wavelet, and the *S* transform, also known as the Stockwell transform (Stockwell *et al.*, 1996), are commonly used methods. Gibson *et al.* (2006) showed that the *S* transform is a special case of the more general CWT using a Morlet-type wavelet, with minor phase and amplitude adjustments.

In this article, we introduce a novel characterization of seismic site response—a TF transfer function TFTF(t, f). The motivation is not to replace the conventional Fourier transfer function but to complement it with the information that is needed when the wavefield contains distinct arrivals that contribute at different times within the same frequency band.

As in our previous works and the works of many other researchers (e.g., Rial, 1996; Kulesh *et al.*, 2005; Burjánek *et al.*, 2010; Poggi *et al.*, 2012; Yang *et al.*, 2020; Aguiar *et al.*, 2026), we use CWT with Morlet wavelet as a tool for TFR computation.

Our study can be outlined as follows. We first recall fundamental relations for TFR. Then, we connect TFR to time- and frequency-domain transfer characteristics, which leads to a definition of TFTF(t, f). Because practical implementation of TFTF(t, f) is not trivial, we also introduce an approximate form *a*TFTF(t, f). Under certain, rather common conditions, *a*TFTF(t, f) sufficiently accurately approximates the exact TFTF(t, f). The important point is that *a*TFTF(t, f) can be computed without modifying commonly used subroutines for CWT.

Finally, we demonstrate a few useful properties of TFTF(t, f) for two selected quasi-1D models of local surface sedimentary structures for which the differences between 1D and 2D responses are only slight and hard-to-detect in $|\mathrm{FTF}(f)|$ but appear much more obvious in $|\mathrm{TFTF}(t,f)|$.

TFR OF A SIGNAL

CWT

The CWT provides a time-scale representation of a signal (Morlet *et al.*, 1982; Grossmann and Morlet, 1984) and is defined as (e.g., Daubechies, 1992)

$$\mathrm{CWT}_{(a,b)}\{s(t)\} := \frac{1}{\sqrt{|a|}}\int_{-\infty}^{\infty} s(t)\ \psi^*\left(\frac{t-b}{a}\right)\mathrm{d}t, \tag{1}$$

with t being time, a the scale parameter, b the translational parameter, and ψ the analyzing wavelet. The asterisk denotes the complex conjugate function.

Given the inverse relationship between scale a and frequency f, the time-scale representation can be interpreted as a TFR.

According to equation (1), at each value of scale a (inversely proportional to frequency f and representing the stretching or compressing of wavelet ψ) and each time b (representing the temporal position of wavelet ψ), wavelet ψ slides over the signal $s(t)$ and measures similarity between them. $\mathrm{CWT}_{(a,b)}\{s(t)\}$ is essentially a localized correlation between the signal and scaled and/or shifted wavelet. Obviously, properties of $\mathrm{CWT}_{(a,b)}\{s(t)\}$ depend on the choice of the analyzing wavelet ψ.

Assuming the Fourier pair in the form

$$\hat{\varphi}(f) \equiv \mathcal{F}_{t\to f}\{\varphi(t)\} := \int_{-\infty}^{\infty} \varphi(\tau)\exp(-\mathrm{i}2\pi f\tau)\mathrm{d}\tau,$$
$$\varphi(t) \equiv \mathcal{F}^{-1}_{f\to t}\{\hat{\varphi}(f)\} := \int_{-\infty}^{\infty} \hat{\varphi}(f)\exp(\mathrm{i}2\pi f t)\mathrm{d}f, \tag{2}$$

equation (1) can be written as

$$\begin{aligned}\mathrm{CWT}_{(a,b)}\{s(t)\} &= \sqrt{|a|}\mathcal{F}^{-1}_{f\to t}\{\hat{s}(f)\ \hat{\psi}^*(af)\}(b)\\ &= \sqrt{|a|}\int_{-\infty}^{\infty}\hat{s}(f)\hat{\psi}^*(af)\exp(\mathrm{i}2\pi f b)\mathrm{d}f.\end{aligned} \tag{3}$$

Finally, let us point out that CWT is advantageous in that it provides a detailed, smoothly varying representation of spectral evolution over time. This facilitates visual interpretation of TFTF(t, f).

CWT with an analytic wavelet

For the present application, we use the complex Morlet wavelet (Grossmann and Morlet, 1984; Goupillaud *et al.*, 1984; Holschneider, 1995)

$$\psi^{\mathrm{M}}(t) = \pi^{-\frac{1}{4}}[\exp(\mathrm{i}\omega_0 t) - \exp(-\omega_0^2/2)]\exp\left(-\frac{1}{2}t^2\right). \tag{4}$$

For sufficiently large ω_0 ($\omega_0 \gtrsim 5.4$), the correction term $\exp(-\omega_0^2/2)$ is numerically very small, and the corrected Morlet wavelet is practically indistinguishable from the simpler Gabor form

$$\psi^{\mathrm{M}}(t) = \pi^{-\frac{1}{4}}\exp(\mathrm{i}\omega_0 t)\exp\left(-\frac{1}{2}t^2\right), \tag{5}$$

that is often used in practical applications. In the same large-ω_0 regime, the wavelet is also commonly treated as approximately analytic (progressive).

The Morlet wavelet is a reasonable choice for a wide class of signals and problems because it provides near-optimal TF localization and yields a smooth, physically interpretable representation of seismic signals. The choice of the ω_0 value affects the time and frequency resolutions in accordance with the Heisenberg–Gabor uncertainty principle—a higher ω_0 improves the frequency resolution at the expense of the time resolution. Therefore, in practical applications, it is important to test different values of ω_0. In the examples in this study as well as in an extensive set of TFTF(t, f) calculations by P. Moczo *et al.* (unpublished manuscript, 2026, see Data and Resources), $\omega_0 = 10$ was found to be a reasonable compromise.

Replace b by t (parameter b corresponds to time) and assume the following relation between the scale parameter a and frequency f (Flandrin, 1999):

$$a = \frac{\omega_0}{2\pi f}. \tag{6}$$

Then, the TFR of signal $s(t)$ based on the CWT and using the Morlet wavelet, say $W\{s(t)\}(t,f)$, can be defined as

$$W\{s(t)\}(t,f) \equiv \mathrm{CWT}_{(f,t)}\{s(t)\} := \sqrt{\frac{2\pi|f|}{\omega_0}} \int_{-\infty}^{\infty} s(\tau)\psi^{\mathrm{M}*}\left(2\pi f \frac{\tau - t}{\omega_0}\right) \mathrm{d}\tau. \tag{7}$$

$W^2\{s(t)\}(t,f)$ represents the energy distribution (energy density) of the signal in the TF plane.

Relation can be expressed using the inverse Fourier transform:

$$\begin{aligned} W\{s(t)\}(t,f) &= \sqrt{\frac{\omega_0}{2\pi|f|}} \mathcal{F}^{-1}_{\xi \to t}\left\{\hat{s}(\xi)\hat{\psi}^{\mathrm{M}*}\left(\frac{\omega_0}{2\pi f}\xi\right)\right\}(t) \\ &= \sqrt{\frac{\omega_0}{2\pi|f|}} \int_{-\infty}^{\infty} \hat{s}(\xi)\ \hat{\psi}^{\mathrm{M}*}\left(\frac{\omega_0}{2\pi f}\xi\right) \exp(\mathrm{i}2\pi\xi t)\mathrm{d}\xi. \end{aligned} \tag{8}$$

This relation is used for numerical computation of TFR based on the CWT and using the Morlet wavelet.

A TF amplitude or envelope $E(t,f)$ and phase $\phi(t,f)$ at a given point of the TF plane can be defined as

$$\begin{aligned} E\{s(t)\}(t,f) &:= |W\{s(t)\}(t,f)| \\ \phi\{s(t)\}(t,f) &:= \mathrm{Arg}[W\{s(t)\}(t,f)]. \end{aligned} \tag{9}$$

Because $W\{s(t)\}(t,f)$ is defined using the CWT with the analytic Morlet wavelet, the envelope E and phase ϕ are consistent with those defined using the analytical signal.

The considered TFR does not suffer from the well-known problems and limitations of the windowed Fourier transform due to the fixed TF resolution of the latter transform.

For numerical computation of the TFR using the CWT and six other methods, there is the publicly available software package TF-SIGNAL in Fortran (Kristekova, Kristek, and Moczo, 2006). A Python version for computation of the CWT is available, for example, at ObsPy: A Python Toolbox for seismology (Krischer *et al.* 2015).

TIME- AND FREQUENCY-DOMAIN TRANSFER CHARACTERISTICS

If the input signal is Dirac delta function in time $\delta(t)$, the time-domain response, the so-called impulse response, say IR(t), fully characterizes (linear, time-invariant) transfer properties between the source and the receiver. The Fourier transform of the IR, the complex Fourier transfer function FTF(f),

$$\mathrm{FTF}(f) := \mathcal{F}_{t \to f}\{\mathrm{IR}(t)\}, \tag{10}$$

fully characterizes the transfer properties in the frequency domain.

As it is well known, in the time-domain numerical-modeling methods, a source signal is discretized in time or in space. Therefore, we cannot apply strictly a Dirac impulse $\delta(t)$ and directly obtain the IR(t). However, we can easily apply some auxiliary signal that we may call a delta-like signal and denote it as DLS(t). An example of such a signal is shown in Figure 1. It is the Gabor signal

$$e(t) \equiv \exp\{-[\omega_p\ t/\gamma_s]^2\} \cos[\omega_p\ t + \theta], \tag{11}$$

with $\gamma_s = 0.065$, $\omega_p = 2\pi 0.45$ rad/s, $\theta = 0$ rad. Parameter γ_s controls the width of the signal, and θ is a phase shift. With a proper choice of parameter values, the Gabor signal is also suitable for simulating a signal with an optionally narrow spectrum centered at a chosen frequency.

A time-domain response to DLS(t) may be called a pseudoimpulse response (PIR) and may be denoted as PIR(t). From PIR(t) and DLS(t) we can obtain the true complex Fourier transfer function:

$$\mathrm{FTF}(f) = \frac{\mathcal{F}_{t \to f}\{\mathrm{PIR}(t)\}}{\mathcal{F}_{t \to f}\{\mathrm{DLS}(t)\}}. \tag{12}$$

The term in the numerator may be called pseudotransfer function $\mathrm{PTF}(f) := \mathcal{F}_{t \to f}\{\mathrm{PIR}(t)\}$. Combining equations (10) and (12), the IR(t) is

$$\mathrm{IR}(t) = \mathcal{F}^{-1}_{f \to t}\left\{\frac{\mathcal{F}_{t \to f}\{\mathrm{PIR}(t)\}}{\mathcal{F}_{t \to f}\{\mathrm{DLS}(t)\}}\right\}. \tag{13}$$

Obviously, these relations have to be treated with care because the amplitude Fourier spectrum of DLS(t) effectively vanishes at higher frequencies, and the numerical evaluation of FTF(f) is limited up to some effective finite frequency. Though IR(t) itself cannot be strictly evaluated in the unlimited frequency range, we will properly use it subsequently.

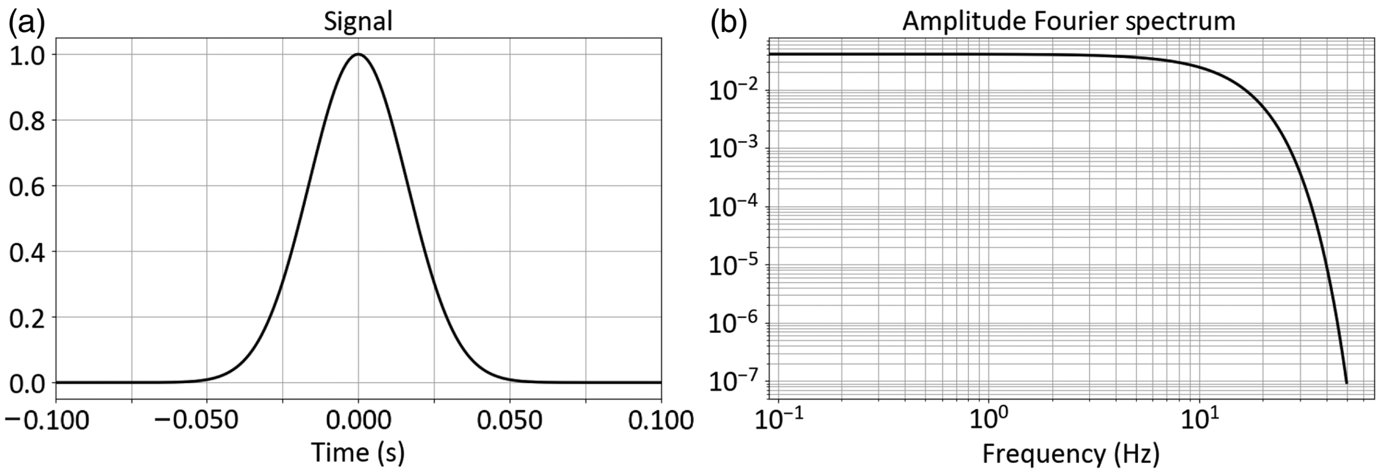

Figure 1. (a) Gabor signal used for obtaining pseudoimpulse response (PIR). (b) Amplitude Fourier spectrum of the signal. The signal can represent any physical time-dependent variable. In the numerical examples of seismic motions in sedimentary structures the signal represents particle velocity in meters per second. Then, the amplitude Fourier spectrum is in meters.

TFTF

Exact formulation

As mentioned in the Introduction, it is reasonable to assume that the possibility to see temporal development of the frequency content of the Fourier transfer function could help to understand and interpret seismic motion in the investigated model of a local surface sedimentary or topographic structure.

Obviously, instead of the Fourier transform of the IR, we need to compute the TFR of the IR. With reference to equation (8), we need to compute $W\{\mathrm{IR}(t)\}(t,f)$. Thus, replacing signal $s(t)$ by $\mathrm{IR}(t)$ in equation (8) and using equation (13) we obtain the complex $\mathrm{TFTF}(t, f)$:

$$\begin{aligned}\mathrm{TFTF}(t,f) &:= W\{\mathrm{IR}(t)\}(t,f)\\ &= \sqrt{\frac{\omega_0}{2\pi|f|}}\mathcal{F}^{-1}_{\xi\to t}\left\{\frac{\mathcal{F}_{t\to\xi}\{\mathrm{PIR}(t)\}}{\mathcal{F}_{t\to\xi}\{\mathrm{DLS}(t)\}}(\xi)\hat{\psi}^{\mathrm{M}*}\left(\frac{\omega_0}{2\pi f}\xi\right)\right\}(t). \quad (14)\end{aligned}$$

Equation (14) includes the ratio of the Fourier transforms of $\mathrm{PIR}(t)$ and $\mathrm{DLS}(t)$. Therefore, as indicated in relation to equation (13), $\mathrm{TFTF}(t, f)$ can be meaningfully and numerically stably evaluated only within the frequency band where the $\mathrm{DLS}(t)$ has nonnegligible spectral energy. In practice, we compute $\mathrm{TFTF}(t, f)$ only up to a maximum frequency $f_{\max}$, defined as the highest frequency at which the spectrum of $\mathrm{DLS}(t)$ remains above a chosen threshold. Beyond $f_{\max}$, the $\mathrm{TFTF}(t, f)$ would become ill-conditioned due to division by near-zero values.

It is advantageous to choose zero-phase delta-like signal $\mathrm{DLS}(t)$ because it avoids an additional time shift that could be uselessly introduced by a signal with nonzero phase.

In analogy with the standard transfer function $|\mathrm{FTF}(f)|$, the TF counterpart is given by $|\mathrm{TFTF}(t,f)|$.

Approximate TFTF

The exact formulation of the $\mathrm{TFTF}(t, f)$ requires computation of the CWT from the ratio of two spectra. Though this does not pose a problem, practically taken, this type of computation is not directly available in standard signal-processing libraries. Therefore, we also introduce an approximate TFTF that can be evaluated without modifying the existing subroutines for CWT calculation.

One may think of analogy with computation of the Fourier transfer function $\mathrm{FTF}(f)$ as the ratio of the Fourier transform of the $\mathrm{PIR}(t)$ and Fourier transform of the delta-like signal $\mathrm{DLS}(t)$—see equation (12). Could the TFTF be analogously computed as the ratio of the TFR of the PIR and TFR of the delta-like signal? No, it cannot.

Certainly, we cannot use an analogy with definition of the Fourier transfer function because in the case of TFR we would divide a function of time and frequency by another function of time and frequency, which could be a problem. The duration of the delta-like signal $\mathrm{DLS}(t)$ is very short whereas duration of the PIR of a local structure can be considerably longer and thus $|W\{\mathrm{DLS}(t)\}(t,f)|$ is close to zero in a major part of the TF plane. Therefore, we cannot simply divide $|W\{\mathrm{PIR}(t)\}(t,f)|$ by $|W\{\mathrm{DLS}(t)\}(t,f)|$.

Considering the $\mathrm{PIR}(t)$, we can evaluate TFR of $\mathrm{PIR}(t)$ and thus its $|W\{\mathrm{PIR}(t)\}(t,f)|$. This can be visualized as a 2D graph in a TF plane. Recall Figure 1b: the amplitude spectrum of $\mathrm{DLS}(t)$ decreases with increasing frequency. Therefore, we have to normalize the frequency content of $|W\{\mathrm{PIR}(t)\}(t,f)|$ by the frequency content of the delta-like signal $\mathrm{DLS}(t)$ used as the input signal for obtaining $\mathrm{PIR}(t)$.

The only reasonable way is to divide the frequency profile of $|W\{\mathrm{PIR}(t)\}(t,f)|$ at each time t by the wavelet equivalent of the amplitude Fourier spectrum of $\mathrm{DLS}(t)$.

Thus, we define an approximation of a complex TFTF, say aTFTF, for any time $t_c \in [t_{\min}, t_{\max}]$ as

$$a\mathrm{TFTF}\{\mathrm{PIR}(t)\}(t_c,f) := \frac{W\{\mathrm{PIR}(t)\}(t_c,f)}{\left[\sqrt{\int_{t_{\min}}^{t_{\max}}|W\{\mathrm{DLS}(t)\}(\tau,f)|^2\mathrm{d}\tau}\right](f)}. \quad (15)$$

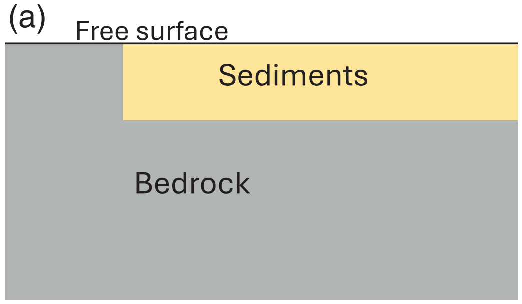

(b)

Material parameters			
Layer			
S-wave speed	β_1	m/s	200
Density	ρ_1	kg/m^3	1900
S-wave quality factor	Q_{S1}		40
Thickness	H	m	25
Bedrock			
S-wave speed	β_2	m/s	1000
Density	ρ_2	kg/m^3	2500
S-wave quality factor	Q_{S2}		100
Theoretical 1D fundamental resonant frequency	$f_0 = \dfrac{\beta_1}{4H}$	Hz	2

Figure 2. (a) Geometry of a 2D model of a semi-infinite sedimentary layer in a bedrock half-space. (b) Material parameters of the model.

This approximation is not identical to the exact TFTF(t,f) in general. Equation (15) replaces the exact pointwise complex deconvolution in the frequency domain with a bandwise normalization based on the wavelet-equivalent amplitude spectrum of the delta-like signal. The aTFTF(t,f) becomes a good proxy for the exact TFTF(t,f) when the delta-like signal is sufficiently impulse-like, so that its amplitude spectrum is nearly constant over the effective passband of the Morlet wavelet centered at f. If the delta-like signal has zero phase, or only linear phase, the remaining difference is limited to normalization and, in the linear-phase case, to a trivial time shift. Therefore, the approximation is meaningful only in the frequency range in which the spectrum of the delta-like signal is nonnegligible.

Computation of aTFTF(t,f) is relatively easy to perform if one has a code for computing wavelet transform $W\{s(t)\}(t,f)$. In the next section, we verify the computation of aTFTF(t,f) according to equation (15) by comparing it with the exact TFTF(t,f) computed according to equation (14).

NUMERICAL VERIFICATION AND EXAMPLES

A model of a semi-infinite sedimentary layer over half-space

Consider the 2D model shown in Figure 2. This simple structure has already been investigated by Moczo and Bard (1993) and revisited recently by Molina-Villegas *et al.* (2018) from a more theoretical viewpoint. It presents the interest to be both close to a 1D structure allowing straightforward interpretations and comparisons, and different enough to generate very peculiar effects with potentially dramatic consequences. Among such consequences, the "damage belt" that occurred during the 1995 Kobe earthquake was interpreted by Kawase (1996) as a special interference effect due to the strong material discontinuity at basin edge. We assume the following orientation of the Cartesian coordinate axes: positive x direction from left to right, positive z direction upward, and positive y direction (⊗) so that (x,y,z) makes the right-handed coordinate system. The wavefield is excited by a vertically incident plane *SH* wave. The particle-velocity vector has the only nonzero component $v_y(x,z,t)$. The input signal representing a particle velocity of the incident wave is Gabor signal specified by equation (11). The parameters of the Gabor signal are suitable for obtaining a PIR in the frequency range [0.1, 20] Hz. Wavelength at 20 Hz in the sedimentary layer is 10 m and we chose grid spacing 0.5 m to assure sufficient accuracy of the numerical simulations. We use the finite-difference (FD) method and FDSim3D code (Kristek and Moczo, 2014; Moczo *et al.*, 2014; Kristek *et al.*, 2019). The code is based on the fourth-order accurate in space and second-order accurate in time staggered-grid FD scheme in the particle-velocity—stress formulation.

Verification of the approximate TFTF

Subject to the conditions described in the previous section, we numerically verified that $|a\mathrm{TFTF}(t,f)|$ is very close to the exact $|\mathrm{TFTF}(t,f)|$. First, we calculated the exact TFTF according to equation (14). Second, we calculated $|a\mathrm{TFTF}(t,f)|$ according to equation (15). We performed these comparisons for several receivers at the free surface of the semi-infinite layer.

Figure 3 shows the exact and approximate TFTFs for receiver at 300 m to the right from the vertical discontinuity of the semi-infinite sedimentary layer. In the chosen frequency range up to 20 Hz, it is practically impossible to see any difference.

Let us emphasize that the theory introduced in this and previous sections is readily applicable to any time-domain IR in different problems of geophysics.

Seismic response atop the semi-infinite sedimentary layer

As shown in Moczo and Bard (1993), when impinged by a vertically incident plane *SH* wave, a 2D *SH* wavefield develops in the semi-infinite attenuating sediment layer, hereafter referred to as the 2D wavefield. For comparison, we also simulated a 1D

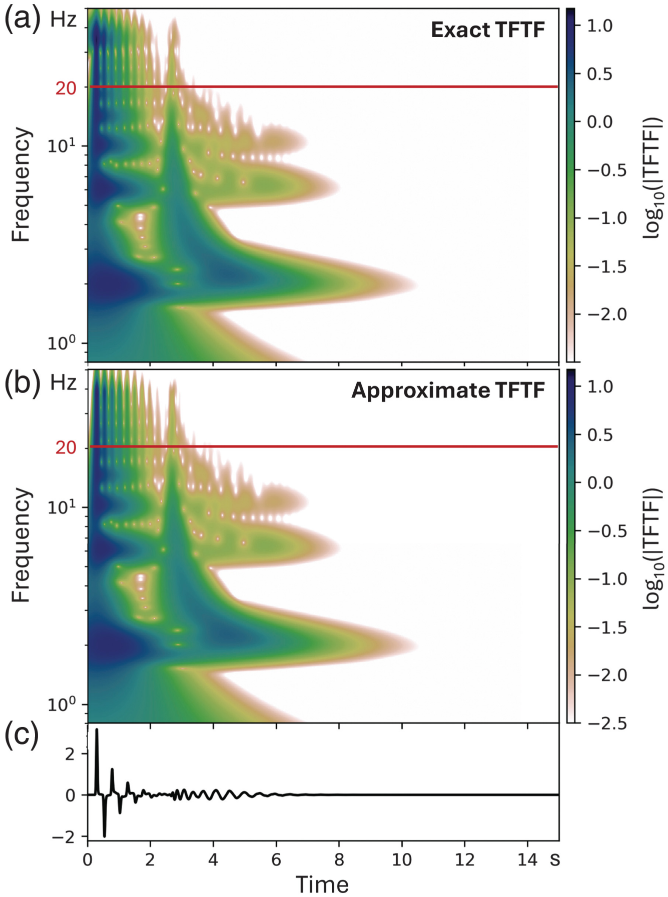

Figure 3. A comparison of the (a) exact $|TFTF(t,f)|$ (top panel) and (b) approximate $|aTFTF(t,f)|$ in the frequency range from 0.8 to 50 Hz, for the (c) velocity time-domain PIR at the receiver located 300 m to the right of the discontinuity. In the frequency range below 20 Hz (below the red line), where the spectrum of the delta-like signal does not deviate from the amplitude at zero frequency by more than one order of magnitude, the differences between the exact and approximate time–frequency (TF) transfer functions (TFTFs) are negligible.

wavefield in an unbounded horizontal sediment layer over a half-space with all other parameters the same as in the model of the semi-infinite layer. That is, we simulated a 1D *SH* vertical resonance in an attenuating sediment layer, hereafter referred to as the 1D resonance. Further, we will consider the corresponding motions at the free surface in both 1D and 2D cases.

In Figure 4a, we show |FTF| for the motion due to the 2D wavefield at a distance of 300 m from the vertical discontinuity of the semi-infinite layer (in solid blue), the same |FTF| smoothed using the Konno–Ohmachi window with parameter $B = 40$ (in solid red), and |FTF| for the motion due to the 1D resonance in the unbounded layer (in solid black). Figure 4b has the same structure as Figure 4a but for a distance of 800 m from the vertical discontinuity. Note that the Konno–Ohmachi smoothing is commonly applied with this $B = 40$ value (e.g., Haghshenas *et al.*, 2008; Theodoulidis *et al.*, 2018), but sometimes even smaller values (30, 20, or even 10) corresponding to stronger smoothing in analysis of earthquake or microtremor ground motion (e.g., Konno and Ohmachi, 1998; Bahrampouri *et al.*, 2021).

The |FTF| for the 1D resonance has a well-known shape with clear peaks corresponding to resonant modes. The raw (i.e., nonsmoothed) |FTF|s qualitatively suggests superposition of 1D resonance and some additional motion(s) and some later arrivals: the later the arrival, the smaller the frequency spacing between the small amplitude ripples around the background 1D resonance shape. The spacing is much smaller at 800 m than at 300 m. Nevertheless, when considering the smoothed |FTF|s, especially at 800 m, these ripples almost disappear, and it is no longer possible to detect and infer the character and occurrence of the additional motions. This is because |FTF| shows only the total spectral content accumulated over the entire duration of the motion. This principal limitation naturally suggests looking at the |TFTF|.

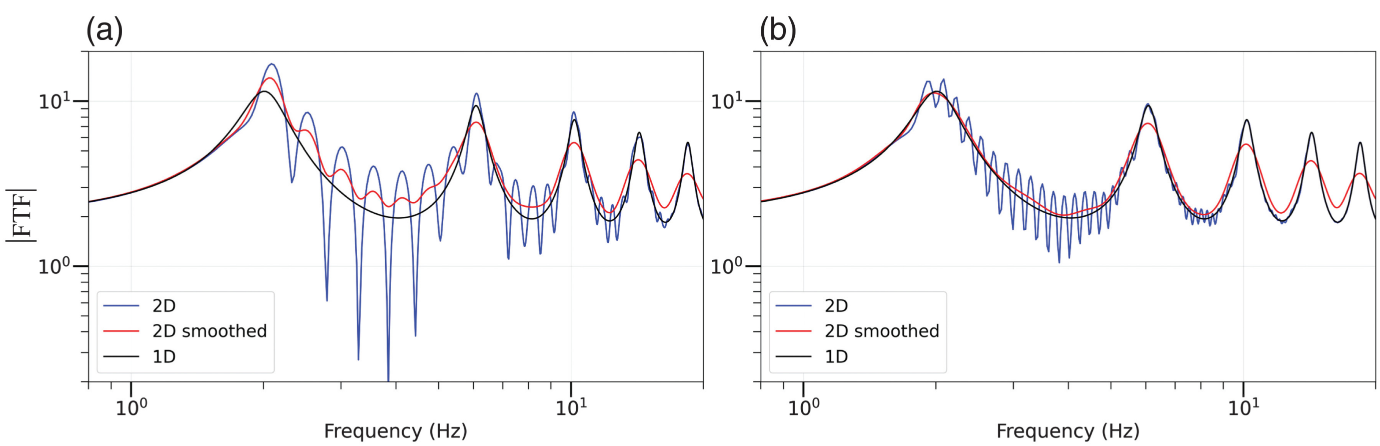

Figure 4. (a) Moduli of the Fourier transfer functions (|FTF|) for the motion due to 2D wavefield at a distance of 300 m from the vertical discontinuity (solid blue), the same |FTF| smoothed (solid red), and |FTF| for the motion due to the 1D resonance in an unbounded layer (solid black). (b) Same as in panel (a) but the 2D-wavefield |FTF|s are for the motion at a distance of 800 m from the vertical discontinuity.

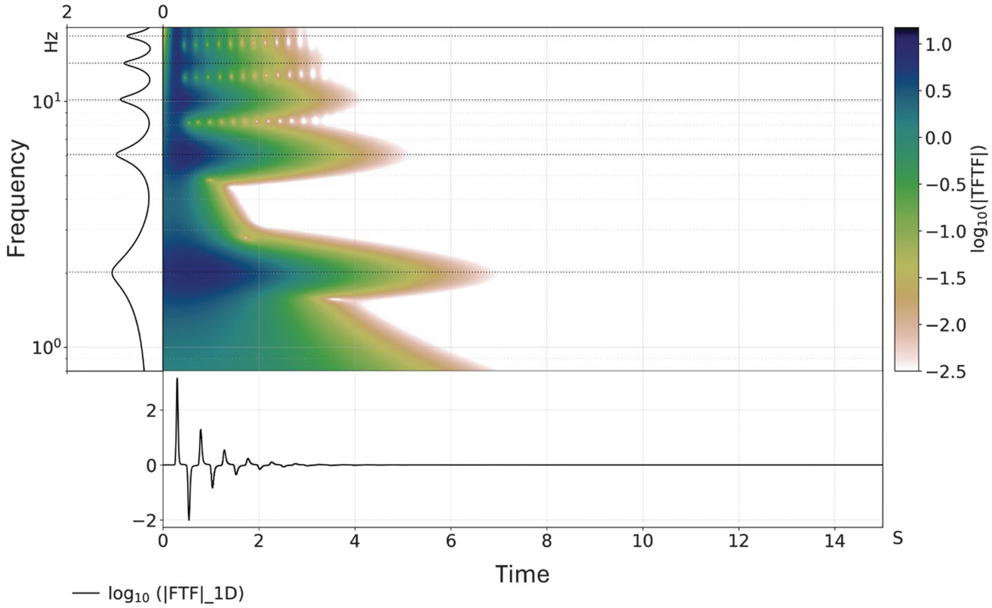

Figure 5. |TFTF| for the surface motion due to 1D wavefield in the horizontal layer over half-space, shown together with the corresponding first five resonant frequencies (horizontal-dotted black lines). The signal beneath the TFTF frame is the particle-velocity PIR for a unit amplitude incident Gabor signal. To the left of the TFTF frame is shown the 1D |FTF| from Figure 4.

Figure 5 shows the "reference" |TFTF| for the 1D case, together with the time-domain PIR (bottom), and the frequency-domain |FTF| (left part). To improve the frequency resolution of the TFTF, we used the Morlet wavelet with the parameter $\omega_0 = 10$. The vertical stripes observed in the |TFTF| (particularly clear at higher frequencies) are not an artifact of the TF analysis. They correspond to the arrival times of multiply reflected *S* waves within the layer, with their time spacing controlled by the layer thickness and the *S*-wave propagation velocity in the sediment. One can clearly identify the five resonance modes in the frequency range [0, 20 Hz], corresponding to the multiply reflected *S* waves within the sedimentary layer. The decrease of duration with increasing mode order (from 6 s at 2 Hz to slightly less than 2.5 s at 18 Hz) is related to the frequency-independent material attenuation, which, for a given travel distance (i.e., a given number of reflections), affects more the high-frequency modes corresponding to shorter wavelengths.

Figure 6 shows PIRs in the v_y component of the particle velocity to the incident *SH* wave. Along the entire profile at the free surface, we can recognize the incident wave followed by a sequence of waves reflected from the sediment-bedrock boundary. The multiple reflections result in the well-known 1D vertical resonance.

When the lower corner of the vertical discontinuity is hit by the incident wave, it becomes an efficient secondary source radiating into all directions affecting the motion in the bedrock and more importantly and significantly inside the sediment layer. The energy propagating along the horizontal and vertical part of the sediment-bedrock interface generates head waves along the respective parts of the interface, propagating inside the layer. The wave radiated in all direction between the vertical and horizontal parts of the interface reaches the free surface and is reflected downward. The reflected wave then reaches the horizontal part of the interface and is reflected upward. This process leads to the generation of a surface Love wave. Part of the energy reflected from the free surface under the critical angle leads to another head wave propagating along the horizontal interface. The upper corner acts similarly with some slight delay.

The resulting wavefield in the layer thus includes not only 1D vertical resonance but also modes of Love wave and a sequence of head waves. The Love wave is well visible in the v_y component of the particle velocity. Head waves are visible as relatively low-amplitude tiny traces. From the PIRs, it is not possible to say more. We can look at |TFTF|s. We select two distances from the vertical discontinuity: 300 and 800 m.

In Figure 7, we show the |TFTF| for the 2D case motion at the same distances of 300 (Fig. 7a) and 800 m (Fig. 7b) from the vertical discontinuity of the semi-infinite layer as in Figure 4. Inside the frame of the |TFTF|, we also show resonant frequencies of the first five modes of the 1D vertical resonance in an unbounded layer (horizontal-dotted black lines) and theoretical arrival times of the first five modes of Love wave propagating in the unbounded layer (solid black). The arrival times are obtained as ratios of the discontinuity-to-receiver distances and the group-velocity values at each frequency, and corrected by the travel time from the source to the free surface. For reference, theoretical dispersion curves of the Love-wave modes in an unbounded horizontal layer are shown in Figure 8. The seismograms beneath the |TFTF| frames are the PIRs. For the direct visual comparison of |TFTF|s and |FTF|s, we also show |FTF|s to the left of the TFTF frames.

It is obvious at the first sight that the |TFTF|s provide substantially better insight into both motions because, contrary to the |FTF|s, they show temporal developments of the spectral contents of the motions. At both distances, we clearly recognize multiple reflections between the free surface and the sediment-layer interface and the resulting 1D resonance pattern at earlier times. The same five resonant frequencies as in the 1D case are

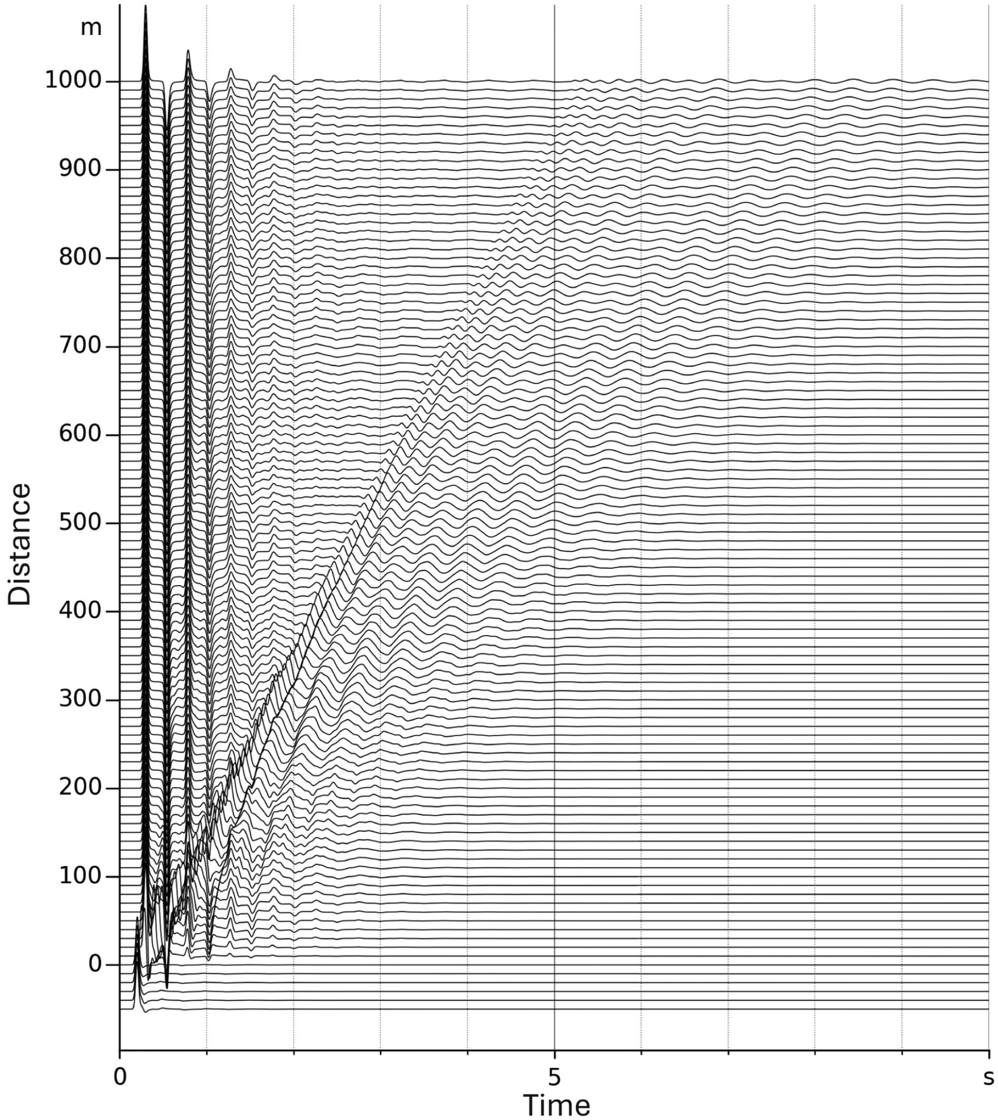

Figure 6. 10-s window of PIRs in v_y component of the particle velocity at the free surface for the vertically incident plane *SH* wave. On the vertical axis, 0 represents the position of the vertical discontinuity (the left vertical boundary of the sedimentary layer), 1000 represents the maximum distance in meters from the vertical discontinuity. The inter-receiver distance is 10 m.

well visible. The 1D resonance groups at both distances are followed by wave groups that dominantly correspond to a laterally propagating surface Love wave generated due to the presence of the vertical discontinuity (left-lateral boundary) of the sediment layer. At distance of 800 m, we see only the fundamental and the first-higher modes of the surface Love wave because the higher modes at this distance vanish due to attenuation. Let us note that these features cannot be seen in the standard |FTF|s. The decrease in duration with mode order is more effective than in the 1D case because the travel distance of Love waves is much longer. Nevertheless, the dominant feature, when comparing the 2D (Fig. 7) and 1D (Fig. 5) cases, is the significant increase of duration. This is particularly obvious for the Airy phases of first two modes, which approximately correspond to the first two 1D resonance frequencies (see the minima in the group velocities shown in Fig. 8b). At 2 Hz, the duration increases from 6 s in the 1D case to 8 s at 300 m from the discontinuity, and up to 13 s at 800 m. At 6 Hz, the durations are around 4.5, 6, and 10 s, respectively.

Layer with randomly undulated interface

As a second example, we consider an unbounded sediment layer over half-space with random smooth undulation of the sediment-bedrock interface. Except the interface undulation, all parameters are the same as in the previous model. The undulation is obtained using a nonsinusoidal stochastic formula $H_{\text{undulated}}(x) = H + z(x)$ with H = 25 m—thickness of the semi-infinite and unbounded layers in the previous numerical example. The zero-mean fluctuation $z(x)$ is Gaussian-correlated with correlation length r = 15 m and bounded by $d = \pm$ 3 m, yielding irregular but laterally coherent undulations. The chosen parameters result in a root mean square variation comparable to that of a sinusoidal profile with an amplitude of 2.5 m and wavelength of 60 m. The model is illustrated in Figure 9. As in the previous example, we consider a 2D *SH* wavefield in the layer due to vertical incidence of the plane *SH* wave from the bedrock.

In Figure 10a, we show |FTF| s in the same way as for the semi-infinite layer in Figure 4 but for the position x = 511 m where the local thickness is exactly the average value of 25 m. The structure of Figure 10b corresponds to that of Figure 6a or 6b except that we omit here theoretical arrival times of the first five modes of Love wave propagating in an unbounded layer with the horizontal interface. Actually, for such an undulating interface, surface waves are generated all along the profile in relation with all thickness irregularities: at any surface receiver, surface waves can come from nearby or more distant

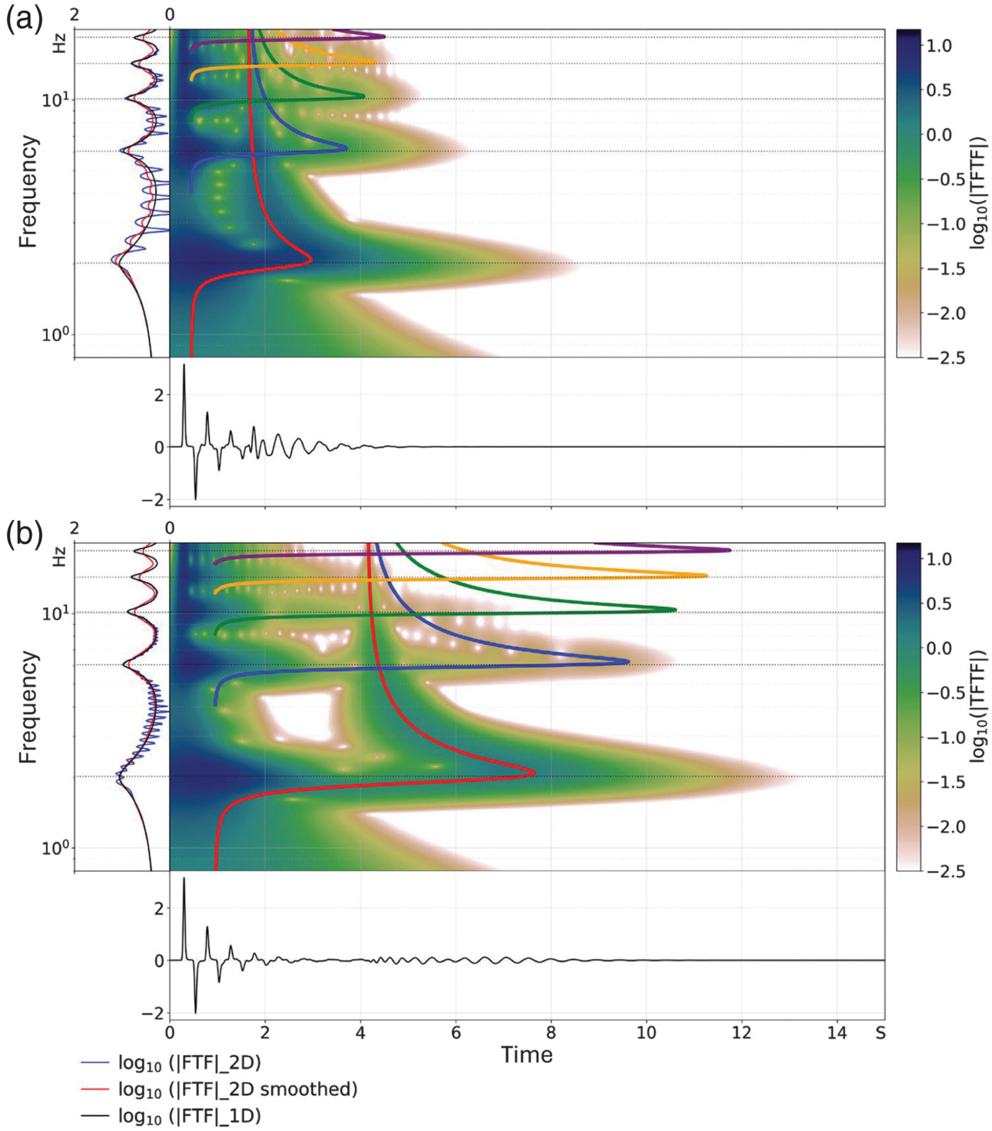

Figure 7. (a) |TFTF| for the motion due to 2D wavefield at distance of 300 m from the vertical discontinuity shown together with resonant frequencies of the first five modes of the 1D vertical resonance (horizontal-dotted black lines) and theoretical arrival times of the first five modes of the Love wave propagating in an unbounded layer (colors correspond to modes shown in Fig. 8). The signal beneath the TFTF frame is the particle-velocity PIR for a unit amplitude incident Gabor signal. To the left of the TFTF frame there are |FTF| s from Figure 4a. (b) Same as Figure 7a but for the distance of 800 m from the vertical discontinuity.

heterogeneities. The "blue" (raw) 2D transfer function exhibits significant differences with respect to the black (1D) one. However, they are rather irregular and difficult to interpret. Moreover, the smoothed (red) transfer function is very hard to distinguish from a purely 1D transfer function. At the same time, |TFTF| shows a pattern similar to the 1D pattern of Figure 5, but with very significant prolongation of motion at and around the resonant frequencies of the first two-three 1D resonance modes, as in the previous semi-infinite layer case. The "diffusion" of energy into frequencies between the resonant frequencies as well as prolongation of motion is due to the scattering effect of the undulated sediment-bedrock interface, as can be seen only in the time-domain PIR with many (small amplitude) spurious arrivals even at early times after the direct arrival. Once again, the key feature seen in the |TFTF| is the very large prolongation of motion around the first two resonance frequencies, exceeding 15 s at 2 Hz and 10 s at 6 Hz. So even though the smoothed 1D and 2D FTF are hardly distinguishable, the differences in |TFTF| between Figures 5 and 10 are very clear: the large prolongation is a marker of the existence of locally diffracted surface waves modifying the wavefield.

CONCLUSIONS

The standard Fourier transfer function |FTF| is widely accepted and used for both theoretical analyses and analyses of real time-domain records, especially for identifying resonance peaks and/or the amplified frequency bands, and the corresponding amplification levels. Nevertheless, it does not provide any information on temporal development of the response, that is, the temporal distribution and the origin of different reverberations that cause amplifications. These amplifications are of particular importance in connection with 2D or 3D effects induced by the local surface and underground geometry.

We propose to go one step beyond with the novel concept of a "TFTF." The theory introduced is readily applicable to any time-domain IR in a broad variety of problems investigated in geophysics. Here, we demonstrate its usefulness for seismic site response studies. For the two examples of quasi-1D underground structures, TFTF proves to be significantly more informative than |FTF| on the composition of the wavefield. We hope to have convinced the reader of the value of TFTF in the numerical modeling of seismic motion and site effects of local surface structures.

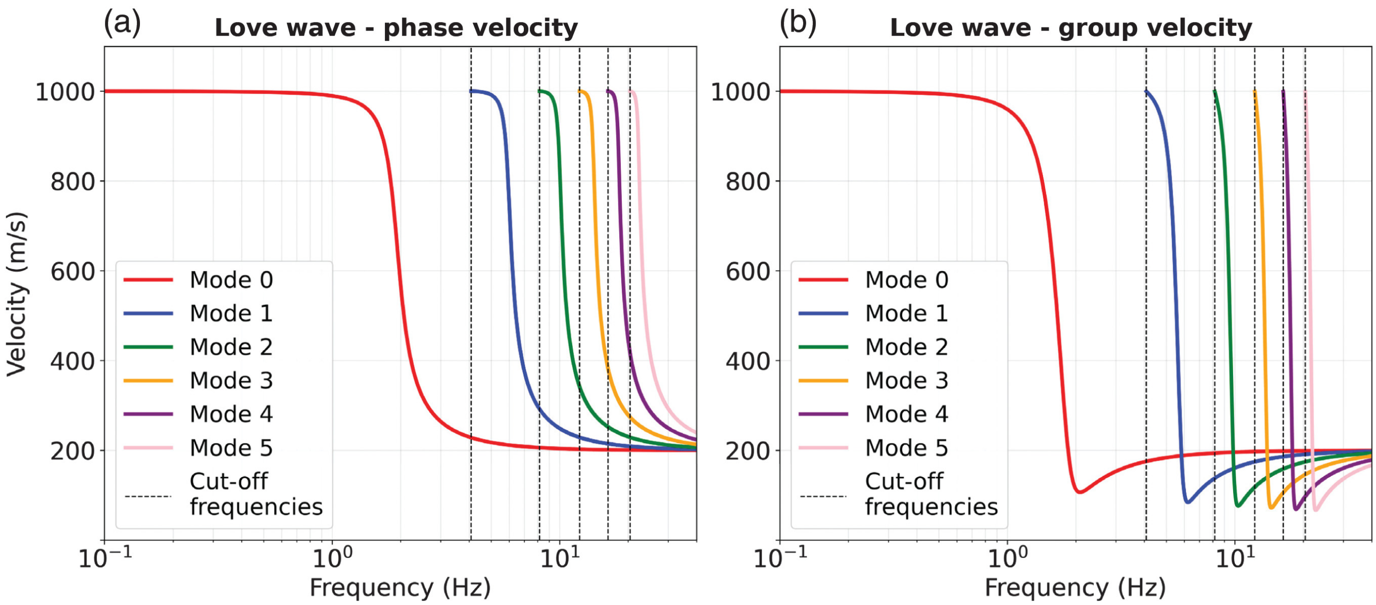

Figure 8. Theoretical dispersion curves of Love-wave modes in an unbounded horizontal sediment layer over half-space: (a) phase velocity and (b) group velocity.

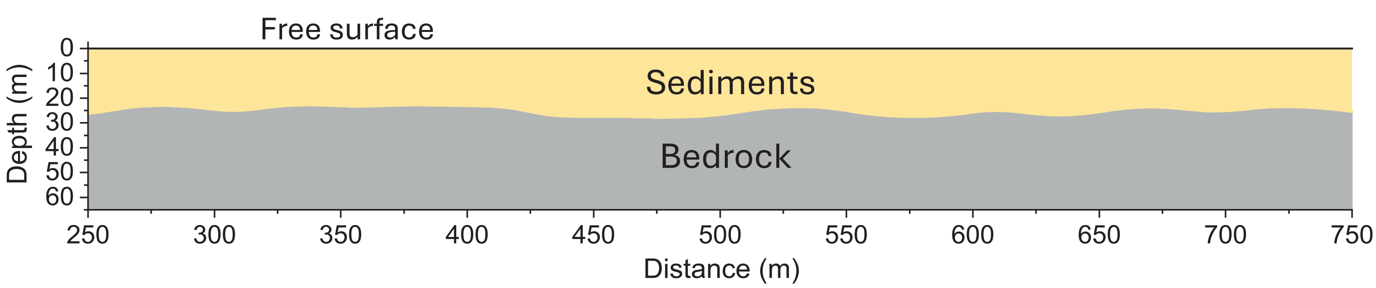

Figure 9. Geometry of a 2D model of an unbounded sediment layer with randomly undulated sediment-bedrock interface. Material parameters of the model are the same as those shown in Figure 2b. Values along the horizontal axis are in meters and correspond to computational model in finite-difference (FD) simulation. 250 m correspond to distance from the left boundary of the FD grid.

TFTF was applied extensively in a study of the translational motion, rotational motion, and axial strain induced in a model of a semi-infinite layer (P. Moczo *et al.*, unpublished manuscript, 2026, see Data and Resources). The next step is to apply the TFTF concept to real recordings. The key issue for that goal is to retrieve robust estimates of the PIR from pairs of earthquake recordings (i.e., at a site under study and a nearby reference site). Significant breakthroughs have been achieved in recent years for borehole arrays (e.g., Mehta *et al.*, 2007; Parolai *et al.*, 2009; Fukushima *et al.*, 2016; Riga *et al.*, 2019), and similar deconvolution and averaging could be considered also when the reference sensor is located at a nearby rock outcrop. This complementary work will be presented soon in a follow-up article, which will address the various processing issues on the example of both realistic synthetics and real recordings from well-known and well-instrumented sites.

DATA AND RESOURCES

There are no new data or resources to report for this article. The unpublished manuscript by P. Moczo, P.-Y. Bard, N. Babaadam, J. Kristek, M. Kristekova, and M. Galis (2026), "Rotational motion and axial strain near a strong lateral discontinuity," submitted to *Geophys. J. Int.*

DECLARATION OF COMPETING INTERESTS

The authors acknowledge that there are no conflicts of interest recorded.

ACKNOWLEDGMENTS

This work was supported by the Slovak Research and Development Agency under the Contract Number APVV-24-0311 (Project SANEFF) and by the Slovak Grant Agency VEGA 2/0050/25. The authors thank two anonymous reviewers and Associate Editor Ricardo Taborda for their comments and suggestions that helped them to improve the original article.

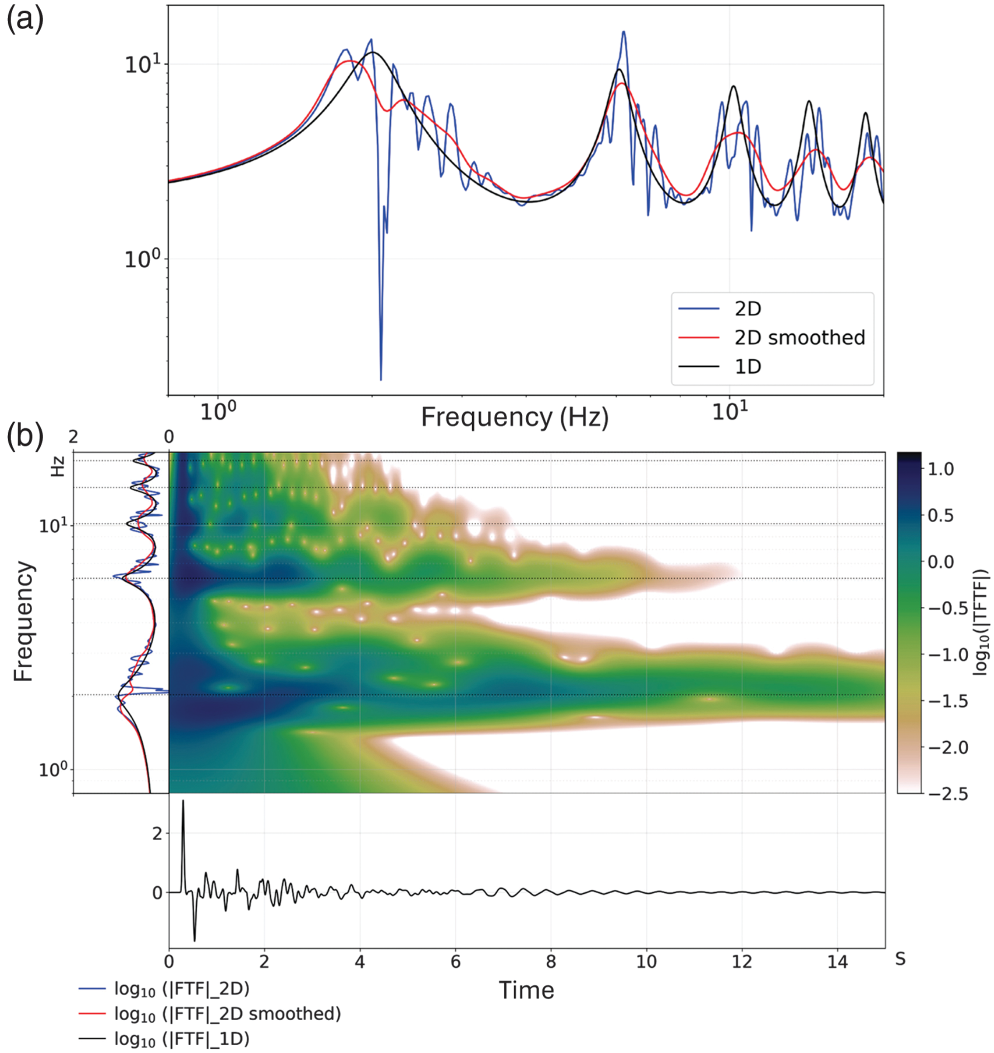

Figure 10. (a) Moduli of the Fourier transfer functions (|FTF|) for the motion due to 2D wavefield at position of 511 m (solid blue), the same |FTF| smoothed (solid red), and |FTF| for the motion due to the 1D resonance in an unbounded layer with horizontal interface (solid black). (b) |TFTF| for the motion due to 2D wavefield at position of 511 m shown together with resonant frequencies of the first five modes of the 1D vertical resonance (horizontal-dotted black lines). The signal beneath the TFTF frame is the particle-velocity PIR for a unit amplitude incident Gabor signal. To the left of the TFTF frame, there are |FTF|s from Figure 10a.

REFERENCES

Aguiar, A. C., A. Chiang, and S. C. Myers (2026). PySolate: A python-based thresholding tool to denoise or designal seismic waveforms based on the continuous wavelet transform, *Seismol. Res. Lett.* **97,** 514–523.

Bahrampouri, M., A. Rodriguez-Marek, S. Shahi, and H. Dawood (2021). An updated database for ground motion parameters for KiK-net records, *Earthq. Spectra* **37,** 505–522.

Basokur, A. T, U. Dikmen, and O. E. Tokgoz (2003). Time-frequency representation of strongmotion records for damage appraisal: Examples from the Düzce earthquake (Turkey), *Near Surf. Geophys.* **1,** 95–101.

Beauval, C., P. Y. Bard, P. Moczo, and J. Kristek (2003). Quantification of frequency-dependent lengthening of seismic ground-motion duration due to local geology: Applications to the Volvi area (Greece), *Bull. Seismol. Soc. Am.* **93,** 371–385.

Birgören, G., and K. Irikura (2005). Estimation of site response in time domain using the Meyer–Yamada wavelet analysis, *Bull. Seismol. Soc. Am.* **95,** 1447–1456.

Bonilla, L. F., P. Guéguen, and Y. Ben-Zion (2019). Monitoring coseismic temporal changes of shallow material during strong ground motion with interferometry and autocorrelation, *Bull. Seismol. Soc. Am.* **109,** 187–198.

Boore, D. M. (2003). Phase derivatives and simulation of strong ground motions, *Bull. Seismol. Soc. Am.* **93,** 1132–1143.

Burjánek, J., G. Gassner-Stamm, V. Poggi, J. R. Moore, and D. Fäh (2010). Ambient vibration analysis of an unstable mountain slope, *Geophys. J. Int.* **180,** 820–828.

Chaljub, E., E. Maufroy, P. Moczo, J. Kristek, F. Hollender, P.-Y. Bard, E. Priolo, P. Klin, F. De Martin, Z. Zhang, *et al.* (2015). 3-D numerical simulations of earthquake ground motion in sedimentary basins: Testing accuracy through stringent models, *Geophys. J. Int.* **201,** 90–111.

Daubechies, I. (1992). *Ten Lectures on Wavelets*, Society for Industrial and Applied Mathematics, Philadelphia, Pennsylvania.

Flandrin, P. (1999). *Time-frequency/Time-scale Analysis*, Academic Press, San Diego, California.

Fukushima, R., H. Nakahara, and T. Nishimura (2016). Estimating S-wave attenuation in sediments by deconvolution analysis of KiK-net borehole seismograms, *Bull. Seismol. Soc. Am.* **106,** 552–559.

Gibson, P. C., M. P. Lamoureux, and G. F. Margrave (2006). Letter to the editor: Stockwell and wavelet transforms, *J. Fourier Anal. Appl.* **12,** 713–721.

Grossmann, A., and J. Morlet (1984). Decomposition of Hardy functions into square integrable wavelets of constant shape, *SIAM J. Math. Anal.* **15,** 723–736.

Goupillaud, P., A. Grossmann, and J. Morlet (1984). Cycle-octave and related transforms in seismic signal analysis, *Geoexploration* **23,** 85–102.

Haghshenas, E., P.-Y. Bard, N. Theodulidis, and , and SESAME WP04 Team (2008). Empirical evaluation of microtremor H/V spectral ratio, *Bull. Earthq. Eng.* **6,** 75–108.

Holschneider, M. (1995). *Wavelets: An Analysis Tool*, Clarendon Press, Oxford, United Kingdom.

Kawase, H. (1996). The cause of the damage belt in Kobe: "The basin-edge effect," constructive interference of the direct S-wave with the basin-induced diffracted/rayleigh waves, *Seismol. Res. Let.* **67,** 25–34.

Konno, K., and T. Ohmachi (1998). Ground-motion characteristics estimated from spectral ratio between horizontal and vertical components of microtremor, *Bull. Seismol. Soc. Am.* **88,** 228–241.

Krischer, L., T. Megies, R. Barsch, M. Beyreuther, T. Lecocq, C. Caudron, and J. Wassermann (2015). ObsPy: A bridge for seismology into the scientific Python ecosystem, *Comput. Sci. Disc.* **8,** 014003, doi: 10.1088/1749-4699/8/1/014003.

Kristek, J., and P. Moczo (2014). FDSim3D – The Fortran95 code for numerical simulation of seismic wave propagation in 3D heterogeneous viscoelastic media, available at www.cambridge.org/moczo (last accessed June 2026).

Kristek, J., P. Moczo, E. Chaljub, and M. Kristekova (2019). A discrete representation of a heterogeneous viscoelastic medium for the finite-difference modelling of seismic wave propagation, *Geophys. J. Int.* **217,** 2021–2034.

Kristekova, M., J. Kristek, and P. Moczo (2006). TF-SIGNAL – program package for or computation and visualization of time-frequency representations of time signals, available at https://www.nuquake.eu/Computer_Codes/TF-SIGNAL.ZIP (last accessed June 2026).

Kristekova, M., J. Kristek, and P. Moczo (2009). Time-frequency misfit and goodness-of-fit criteria for quantitative comparison of time signals, *Geophys. J. Int.* **178,** 813–825.

Kristekova, M., J. Kristek, P. Moczo, and S. Day (2006). Misfit criteria for quantitative comparison of seismograms, *Bull. Seismol. Soc. Am.* **96,** 1836–1850.

Kristekova, M., P. Moczo, P. Labak, A. Cipciar, L. Fojtikova, J. Madaras, and J. Kristek (2008). Time-frequency analysis of explosions in the ammunition factory in Novaky, Slovakia, *Bull. Seismol. Soc. Am.* **98,** 2507–2516.

Kulesh, M. A., M. S. Diallo, and M. Holschneider (2005). Wavelet analysis of ellipticity, dispersion, and dissipation properties of Rayleigh waves, *Acoust. Phys.* **51,** 425–434.

Kuyuk, H. S. (2015). On the use of Stockwell transform in structural dynamic analysis, *Sadhana* **40,** 295–306.

Maufroy, E., E. Chaljub, F. Hollender, J. Kristek, P. Moczo, P. Klin, E. Priolo, A. Iwaki, T. Iwata, V. Etienne, *et al.* (2015). Earthquake ground motion in the Mygdonian basin, Greece: The E2VP verification and validation of 3D numerical simulation up to 4 Hz, *Bull. Seismol. Soc. Am.* **105,** 1398–1418.

Maufroy, E., E. Chaljub, F. Hollender, P.-Y. Bard, J. Kristek, P. Moczo, F. De Martin, N. Theodoulidis, M. Manakou, C. Guyonnet-Benaize, *et al.* (2016). 3D numerical simulation and ground motion prediction: Verification, validation and beyond – Lessons from the E2VP project, *Soil Dynam. Earth. Eng.* **91,** 53–71.

Mehta, K., R. Snieder, and V. Grazier (2007). Downhole receiver function: A case study, *Bull. Seismol. Soc. Am.* **97,** 1396–1403.

Moczo, P., and P.-Y. Bard (1993). Wave diffraction, amplification and differential motion near strong lateral discontinuities, *Bull. Seismol. Soc. Am.* **83,** 85–106.

Moczo, P., J. Kristek, P.-Y. Bard, S. Stripajová, F. Hollender, Z. Chovanová, M. Kristekova, and D. Sicilia (2018). Key structural parameters affecting earthquake ground motion in 2D and 3D sedimentary structures, *Bull. Earthq. Eng.* **16,** 2421–2450.

Moczo, P., J. Kristek, and M. Galis (2014). *The Finite-difference Modelling of Earthquake Motions: Waves and Ruptures*, Cambridge University Press, Cambridge, United Kingdom.

Molina-Villegas, J. C., J. D. Jaramillo-Fernández, J. Piña-Flores, and F. J. Sánchez-Sesma (2018). Local generation of love surface waves at the edge of a 2D alluvial valley, *Bull. Seismol. Soc. Am.* **108,** 2090–2103.

Morlet, J., G. Arens, E. Fourgeau, and D. Giard (1982). Wave propagation and sampling theory; Part I, Complex signal and scattering in multilayered media, *Geophysics* **47,** 203–221.

Nigam, N. C. (1984). Phase properties of earthquake ground acceleration records, *Proc. Eighth World Conf. on Earthquake Engineering*, Vol. 2, Prentice Hall, New York, New York, 549–556.

Ohsaki, Y. (1979). On the significance of phase content in earthquake ground motions, *Earthq. Eng. Struct. Dynam.* **7,** 427–439.

Paolucci, R. (1999). Numerical evaluation of the effect of cross-coupling of different components of ground motion in site response analyses, *Bull. Seismol. Soc. Am.* **89,** 877–887.

Parolai, S., A. Ansal, S. Kurtulus, A. Strollo, R. Wang, and J. Zschau (2009). The Ataköy vertical array (Turkey): Insights into seismic wave propagation in the shallow-most crustal layers by waveform deconvolution, *Geophys. J. Int.* **178,** 1649–1662.

Poggi, V., D. Fäh, J. Burjanek, and D. Giardini (2012). The use of Rayleigh-wave ellipticity for site-specific hazard assessment and microzonation: Application to the city of Lucerne, Switzerland, *Geophys. J. Int.* **188,** 1154–1172.

Rial, J. A. (1996). The anomalous seismic response of the ground at the Tarzana hill site during the Northridge 1994 southern California earthquake: A resonant, sliding block?, *Bull. Seismol. Soc. Am.* **86,** 1714–1723.

Riga, E., F. Hollender, Z. Roumelioti, P.-Y. Bard, and K. Pitilakis (2019). Assessing the applicability of deconvolution of borehole records for determining near-surface shear wave attenuation, *Bull. Seismol. Soc. Am.* **109,** 621–635.

Sawada, T. (1984). Application of phase differences to the analysis of nonstationarity of earthquake ground motion, *Proc. Eighth World Conf. Earthquake Engineering*, Vol. 2, Prentice Hall, New York, New York, 557–564.

Stockwell, R. G., L. Mansinha, and R. P. Lowe (1996). Localization of the complex spectrum: the S transform, *IEEE Trans. Signal Process.* **44,** 998–1001.

Theodoulidis, N., G. Cultrera, C. Cornou, P.-Y. Bard, T. Boxberger, G. DiGiulio, A. Imtiaz, D. Kementzetsidou, K. Makra, and , and the Argostoli NERA team (2018). Basin effects on ground motion: The case of a high-resolution experiment in Cephalonia (Greece), *Bull. Earthq. Eng.* **16,** 529–560.

Yamamoto, Y., and J. W. Baker (2013). Stochastic model for earthquake ground motion using wavelet packets, *Bull. Seismol. Soc. Am.* **103,** 3044–3056.

Yang, Y., C. Liu, and C. A. Langston (2020). Processing seismic ambient noise data with the continuous wavelet transform to obtain reliable empirical Green's functions, *Geophys. J. Int.* **222,** 1224–1235.

Manuscript received 2 March 2026
Published online 30 June 2026